International Journal of Heat and Mass Transfer 51 (2008) 5368–5379

Contents lists available at ScienceDirect

International Journal of Heat and Mass Transfer

journal homepage: www.elsevier.com/locate/ijhmt

Comprehensive experimental and theoretical study of fluid flow and heat transfer in a microscopic evaporating meniscus in a miniature heat exchanger

Sashidhar S. Panchamgam [1], Arya Chatterjee, Joel L. Plawsky, Peter C. Wayner Jr. *

The Isermann Department of Chemical and Biological Engineering, Rensselaer Polytechnic Institute, Troy, NY 12180, USA

ARTICLE INFO

Article history:
Received 22 May 2007
Received in revised form 21 March 2008
Available online 18 May 2008

Keywords:
Capillary forces
Evaporating meniscus
Heat conduction
Marangoni stresses
Miniature heat pipe
Slip modeling

ABSTRACT

The complex physicochemical phenomena occurring in the contact line region of an evaporating meniscus are described using a unique combination of high-resolution experimental data and three complementary models. The following were used: (1) high-resolution experimental liquid profile data (thickness, slope, curvature and curvature gradient) to obtain the pressure gradient in the evaporating pentane meniscus in a vertical constrained vapor bubble (VCVB); (2) macroscopic outside surface temperature profile data; (3) a finite element model to obtain the two-dimensional heat conduction profile in the solid substrate wall (macro-model) and the solid–liquid interfacial temperature profile in the evaporating meniscus region; (4) a continuum fluid-dynamics model (micro-model) to obtain the liquid–vapor interfacial temperature, mass flow rate, Marangoni stresses, and evaporative heat flux profiles along the length of the evaporating meniscus; and (5) the Kelvin–Clapeyron model to obtain the vapor temperature profile (liquid–vapor interfacial temperature jump) in the evaporating meniscus region.
The retarded dispersion constant and high-resolution thickness, slope, curvature and curvature gradient profiles were obtained from the experimental reflectivity profiles. There was a substantial increase in the measured curvature in the transition region, where the evaporation rate and flux are a maximum. To obtain numerical closure between the three complementary models, the continuum fluid dynamics model (micro-model) required slip at the solid–liquid interface to support the observed high mass flow rates in the evaporating pentane meniscus. Mass flow rates due to Marangoni stresses, capillary pressure and disjoining pressure are compared. Depending on the liquid thickness, Marangoni stresses can either enhance or hinder fluid flow towards the contact line for the evaporating pure pentane meniscus. Due to the high heat removal rate by the evaporating pentane meniscus in the transition region, dips in the vapor, liquid–vapor and solid–liquid interface temperature were obtained. The results demonstrate and describe the sensitivity and complexity of the phase change process in micro-regions.

1. Introduction

The study of an evaporating meniscus on a solid substrate is important to many applications involving phase change phenomena, like miniature heat pipes, nucleate boiling, coatings, etc. In particular, for miniature heat pipes and boiling, the presence of a high heat flow rate is due to the enormous heat flux that occurs in the contact line region of the evaporating curved film. As demonstrated herein, both the resistances to the converging heat flow in the solid substrate and to the converging evaporating liquid flow in the meniscus are important. In our previous papers we did not include the effect of a detail analysis of conduction in the substrate. Herein, using experimental data, we combine a finite element analysis of two-dimensional heat conduction in the substrate with an analysis of fluid flow in the meniscus to give a comprehensive view of the phenomena controlling an evaporating meniscus. Since this paper complements previous papers in which comprehensive experimental data on the meniscus profile were presented [1–3], these previously presented experimental results are only overviewed below for completeness. However, additional experimental data on the outside temperature profile are now presented which allows the complementary analysis of converging heat flow in the solid. Although there are many modeling papers in the literature, there are only a few papers that present modeling results for menisci profiles that are substantiated by experimental data for the temperature (e.g., [4]). We find that to obtain agreement between the details of heat conduction in the substrate and the details of fluid evaporation in the meniscus, a slip velocity at the liquid–solid interface is needed. It has been well known for many years that non-Newtonian liquids can show effective slip at solid surfaces. For a more relative system, Spikes and Granick have demonstrated slip using a simple isothermal non-evaporating fluid on a

* Corresponding author. Tel.: +1 518 276 6199; fax: +1 518 276 4030.
E-mail address: wayner@rpi.edu (P.C. Wayner Jr).
[1] Present address: Intel, 2501 NW 229th Avenue, Hillsboro, OR 97124, USA.

0017-9310/$ - see front matter © 2008 Elsevier Ltd. All rights reserved.
doi:10.1016/j.ijheatmasstransfer.2008.03.023

Nomenclature

a, b	constants for surface tension of pure fluids
B_{avg}	average dispersion constant (experimental) (J m)
g	acceleration due to gravity (m/s^2)
h_{fg}	heat of vaporization (J/kg)
k_l	thermal conductivity of the liquid (W/m K)
K	curvature (m^{-1})
P	pressure (Pa)
P_{vT}	total pressure in the vapor phase (Pa)
q''	heat flux (W/m^2)
q''_{ev}	evaporative heat flux (W/m^2)
Q_{in}	heater power input (W)
t	time (s)
T	temperature (K)
T_{lv}	liquid–vapor interface temperature (K)
T_{sl}	solid–liquid interface temperature (K)
T_v	vapor temperature (K)
x	length of the cuvette (m)
y	distance perpendicular to the length of the cuvette, x (m)

Greek symbols

α	fitting constant (m^{-2})
β	slip coefficient (m)
δ	film thickness (m)
δ_0	adsorbed film thickness (m)
Γ	mass flow rate per unit width (kg/m s)
λ	wavelength (m)
μ	dynamic viscosity (kg/m s)
υ	kinematic viscosity (m^2/s)
Π	disjoining pressure (Pa)
ρ_l	liquid density (kg/m^3)
$\Psi_{0.1\,\mu m}$	distance traveled by the meniscus (m)
σ	surface tension (N/m)
τ_{yx}	shear stress at the liquid–vapor interface (N/m^2)

Subscripts

avg	average
ev	evaporating meniscus region
l	liquid
lm	liquid molar amount
sl	solid–liquid interface
lv	liquid–vapor interface
w	outside cuvette wall

Superscript

$'$	derivative with respect to x

completely wetting surface in a surface force apparatus, SFA [5]. In their experiments, the film thicknesses and high shear stresses were comparable to a portion of an evaporating meniscus in the contract line region. Extensive discussions of the literature on the slip velocity are given in [5–7].

Herein, we study a portion of a relatively large transparent wickless heat pipe with four corner grooves, which should be a very effective passive fin heat exchanger based on capillarity in a microgravity environment where gravitational effects are minimal. In the earth's environment, we find that it is a good research tool to study the details of change-of-phase heat transfer in small systems. A similar set-up is destined to fly aboard the International Space Station and these results will be compared with our earth-bound experiments. The heat pipe consists of a vertical quartz cuvette partially filled with pentane so that it traps some vapor at the top (see Fig. 1) giving a VCVB. Not only does this set-up enable us to look closely at the contact line region with great magnification, but also provides us with a platform for other relevant studies like wetting, spreading and the exploration of droplets with phase change. In addition to the applied heat pipe use, the transparent experimental cell design has the following two basic uses, which are demonstrated herein: (1) under equilibrium conditions, the cell can be used to determine the equilibrium interfacial properties of an extended meniscus in situ and (2) under non-equilibrium conditions, the cell can be used to study fluid flow and transport processes in the contact line region. The data analysis procedure directly gives the slope, film thickness and curvature profiles of an evaporating thin film with high-spatial and temporal resolution. Therefore, these quantities become independent of theoretical models. This has allowed us to calculate the liquid pressure profile, fluid flow and heat flux across the interface with the same spatial resolution. The richness of the data obtained is truly unique in this field of research. These results demonstrate and describe the sensitivity and complexity of the phase change process in small regions.

Fig. 1(c) shows a meniscus formed by a perfectly wetting fluid in contact with a vertical solid substrate. The meniscus can be divided into three regions based on its evaporation rate and the liquid film thickness [8]: (1) *The adsorbed thin film region*, wherein the liquid film thickness is <100 nm and is formed due to the adsorption of the liquid on the solid substrate (during evaporation, we expect negligible or zero evaporation in the adsorbed film region due to the lower vapor pressure caused by the intermolecular forces of attraction between the liquid and the solid); (2) *The evaporating thin film region or the transition region*, wherein maximum evaporation at the liquid–vapor interface is experienced; and (3) *The bulk or thicker meniscus region*, which acts as a reservoir for the liquid evaporated in the transition region (in the bulk meniscus region, the liquid evaporation flux is considerably smaller due to the larger thickness of the liquid film). The liquid pressure field in the film thickness range 10 nm < δ < 4 μm, which is called the micro-model region herein, is measured and analyzed. Since the measurement of the temperature profile is at a larger scale, the analysis of the temperature profile in the solid is called a macro-model.

The concept of disjoining pressure was first proposed by Derjaguin and Churaev (e.g., [9]) as a thermodynamic concept to account for the intermolecular attraction between the solid substrate and the liquid thin film. Using this concept, they showed that the equilibrium thickness of an ultra-thin film is dependent on the interfacial temperature jump [10]. This led to the formulation of the Kelvin–Clapeyron equation for the description of the above three regions by Potash and Wayner [8], wherein the mathematical singularity at the leading edge of an evaporating meniscus was eliminated by showing the presence of a thin adsorbed film of liquid in which the vapor pressure was effected by liquid–solid intermolecular forces. Thus the shape of the meniscus was directly related to the liquid pressure profile and hence to the fluid flow occurring in the thin wedge formed by the liquid. The evaporation at the liquid–vapor interface was in turn dependent on this flow which altered the liquid thickness profile of the meniscus. The Kelvin–Clapeyron formulation provided the necessary boundary condition for the free boundary problem that arose while describing the evaporation at the liquid–vapor interface. The solution to the problem of fluid flow and heat transfer of an evaporating meniscus demonstrated that the direction of the fluid flow is from the intrinsic or the thicker meniscus region to the thin film region and confirmed the existence of a heat flux maximum in a small region adjacent to the

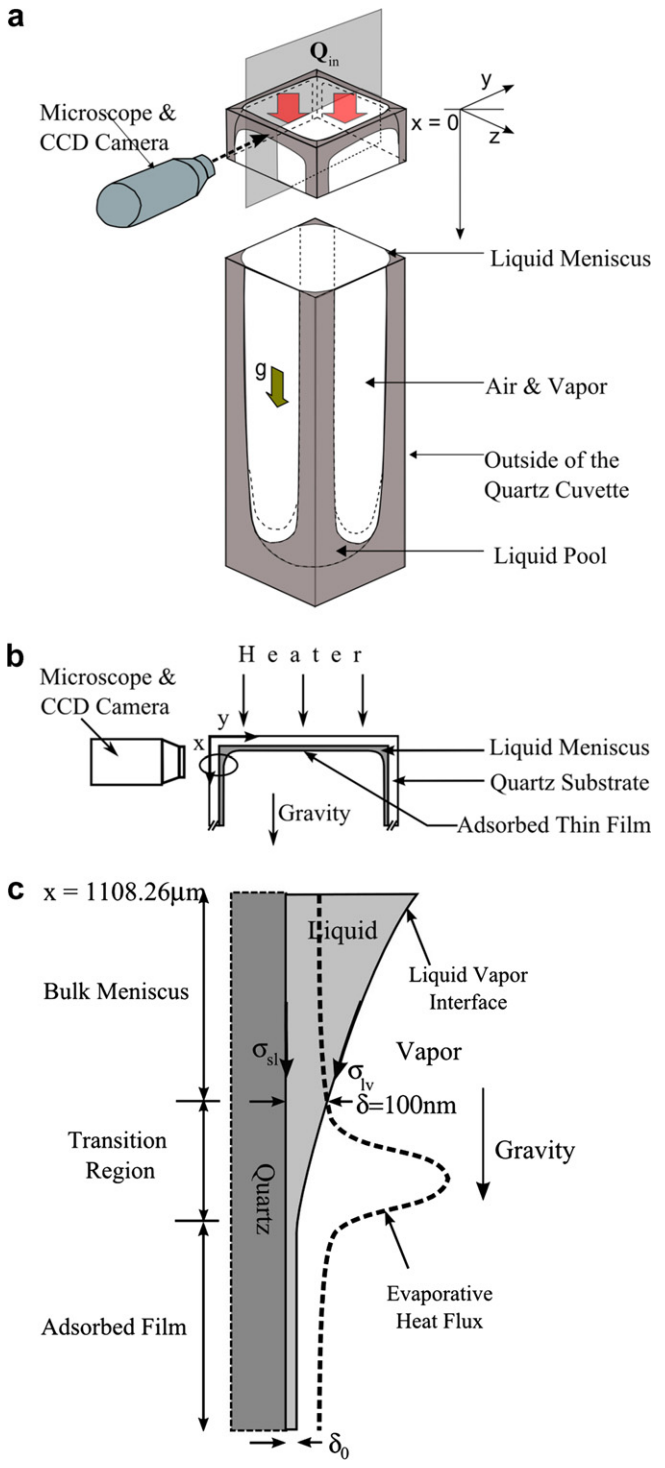

Fig. 1. (a) Schematic representation of the experimental set-up of the VCVB heat exchanger, (b) cross-sectional view of the top-corner of the cuvette showing liquid meniscus and the adsorbed thin film region and (c) schematic of the micro-region.

contact line called the transition region. Extensive literature reviews of these phenomena are given in [1–4,6–12].

A common shortcoming in most of the theoretical models is the availability of high-resolution experimental data for comparison. Herein, we present an overview of our high-resolution experimental data [1–3], i.e., thickness, slope, curvature and curvature gradient, as a function of meniscus length with a horizontal resolution of 0.177 μm in Section 2. These profiles provide important details such as the significant peak in the curvature of the liquid–vapor interface in the transition region. The maximum in the curvature is important to the correct description of the mass flow rate in an evaporating meniscus, which in turn determines the heat removal efficiency of an evaporating meniscus. Using the isothermal experimental data, an in situ measurement of the retarded dispersion constant used in calculating the disjoining pressure was obtained. Panchamgam et al. [2] have shown that the presence of impurities and extremely small particles in the liquid and on the solid surface can significantly alter the wetting properties and the retarded dispersion constant. Hence, by using the isothermal retarded dispersion constant obtained in situ from the experiments, the deviations observed in the experiments, which would not be accounted for in a completely theoretical work, are explained. We note that we use the experimentally obtained profiles for thickness, slope and curvature as inputs to a model instead of solving for thickness as an unknown parameter.

In Section 3.1, where the two-dimensional heat conduction model for heat transfer in the solid region is presented, the fluid mechanics and heat transfer at the microscopic scale of the corner meniscus are coupled with the macro-modeling of heat flow in the macroscopic scale of the solid substrate. Then the continuum mechanics model describing an evaporating meniscus is presented in Sections 3.2 and 3.3. As described in Section 4, this is paired with the finite element model of the solid by imposing appropriate boundary conditions by using an iterative scheme to obtain a converged solution. Therefore, we are able to obtain profiles for all the variables in an evaporating curved film. For example, the Kelvin–Clapeyron model clearly explains the local variation of the vapor temperature, which is usually assumed to be a constant or equal to the room temperature. The comprehensive results of all the aspects involved in an evaporating meniscus existing in a wickless heat pipe are finally presented in Section 5.

2. Overview of experimental work [1,2]

2.1. Experimental set-up

Since this paper complements [1,2], only a brief overview of these experiments is given here for completeness. The experimental set-up presented in Fig. 1 was designed to evaluate the details of an evaporating meniscus in a VCVB heat exchanger. The clean cuvette, was made of fused silica (square cross-section, inside dimensions 3 mm × 3 mm, outside dimensions 5 mm × 5 mm, length 43 mm). To avoid potential contaminants, the previously used pressure transducer and vacuum system was eliminated. The cuvette was filled with pentane (Fluka Chemicals®, purity greater than 99.8%) inside a glove bag under ultra-pure nitrogen environment and was sealed from the bottom using a Teflon stopper. Therefore, the pentane meniscus was in contact with a mixture of its vapor and non-condensable gases at atmospheric pressure. A thermoelectric heater was attached at the top end of the cuvette. To measure the axial temperature profile on the outer side (the side exposed to the room atmosphere) of the cuvette, a series of thermocouples (K type) were attached along the length of the quartz cuvette (x). The entire cuvette assembly was attached to a precision, three-way translation stage on an air-buffered vibration control bench. The translation stage allowed us to focus the microscope at any desired position along the extended meniscus formed in the corners of the cuvette (see Fig. 1(a)).

2.2. Experimental procedure

In the experimental system, liquid from the pool at the bottom of the cuvette rises along the corners of the cuvette due to capillary and disjoining pressure forces and thereby forms a continuous extended

meniscus in all the corners of the cuvette (see Fig. 1(c)). The meniscus formed in one of the top corners was observed. A co-ordinate system with the outside top of the cuvette at $x = 0$ was used. Therefore, the top corner meniscus starts at $x = 1$ mm (the thickness of the cuvette wall being 1 mm). Since the curvature of the bulk meniscus at the top corner is $K \approx 9236.5\ m^{-1}$, the radius of the corner meniscus is 108.26 μm. Thus the approximate position of the thinner portion of the meniscus observed in Fig. 2 is $x = 1108.26$ μm. To study fluid flow and evaporation, we changed the heater power from an isothermal reference state, $Q_{in} = 0$, to a non-isothermal state, $Q_{in} = 0.076$ W. For pentane, the change in the heater power induced a characteristic meniscus movement. The entire meniscus movement due to the step change in the heat input was captured using a CCD camera and a microscope. Monochromatic light (wavelength, $\lambda = 546$ nm) from a mercury light source was used to illuminate the cuvette through the objective of the microscope. Naturally occurring interference fringes appeared (see Fig. 2), which were due to the interaction of the light reflected from the liquid–vapor and the liquid–solid interfaces. A CCD camera with a maximum frame rate of 30 frames per second was used to capture the reflectivity images of the receding and advancing menisci. The captured images were digitized using a data acquisition card (DT3155-MACH Series Frame Grabber) to give high-resolution thickness profiles. Eventually, the evaporating pentane meniscus reached a pseudo-steady state for time, $t > 50$ s (Fig. 2(d)). The pseudo-steady state is defined as a very slow advancement of the meniscus. A more detailed discussion on the meniscus movement is provided in Refs. [1,2]. As our primary focus in this paper is on the modeling of an evaporating steady-state pentane meniscus, we restrict the high-resolution experimental data and the subsequent modeling to the non-isothermal evaporating pentane meniscus in the pseudo-steady state regime at time, $t = 163.2$ s.

2.3. Data analysis

Fig. 3(a) shows the thickness profile of the non-isothermal pentane meniscus during the pseudo-steady state ($t = 163.2$ s). The estimation of the thickness profiles from the raw gray value data measured from the continuous reflectivity profile and interference fringes is explained in detail in Ref. [11]. The horizontal resolution of each pixel used to measure the continuous variation in the reflectivity is 0.177 μm. The thickness decreased (from $\delta = 2.3$ μm as $x \to 1108.26$ μm) with increasing x to the adsorbed film region with a constant thickness of 34 nm (δ_0) at $x \approx 1108.26 + 25$ μm. To obtain the pressure gradient and the Marangoni stresses existing along the length of an evaporating meniscus, the first (δ'), second (δ''), third (δ''') and fourth (δ'''') derivatives of the thickness profile, $\delta(x)$, need to be determined. The thickness profile represented in Fig. 3(a) contained noise. Therefore, a smoothing spline approximation with tolerance (tol) given by, $\text{tol} = \alpha\delta^4$ (where α is a constant), was used to remove noise in the raw thickness data and to make the fitting differentiable. The value of α was determined such that the absolute error in the curve fitting was within 3% and δ''', δ'''' and piece-wise continuous. To check the sensitivity to accuracy ratio, we observed that for 1% change in the relative error in the thin film region, the δ''' changed by 2.5%. The reader should note that the profiles, i.e., thickness, slope and curvature thus obtained for the pentane meniscus during non-isothermal pseudo-steady state, are numerically represented by their respective spline functions making them continuous and differentiable everywhere. Fig. 3(b) represents the slope of the thickness profile obtained from the spline approximation. As the thickness of the film decreases with increase in the distance, the slope is negative. The slope becomes zero in the adsorbed film region ($x \to 1108.26 + 25$ μm). A plot of the local curvature with respect to distance is shown in Fig. 3(c). The curvature is approximately constant in the thicker meniscus region and zero in the adsorbed film region. We measured a significant maximum in the curvature ($K_{max} = 24{,}072\ m^{-1}$) in the transition region ($\delta_0 < \delta < 0.1$ μm). This considerable maximum in the curvature was observed for pure fluids due to evaporation at the liquid–vapor interface but not for a binary mixture of 98% pentane and 2% octane [3]. Marangoni flow due to distillation caused a significant difference in the results with the mixture.

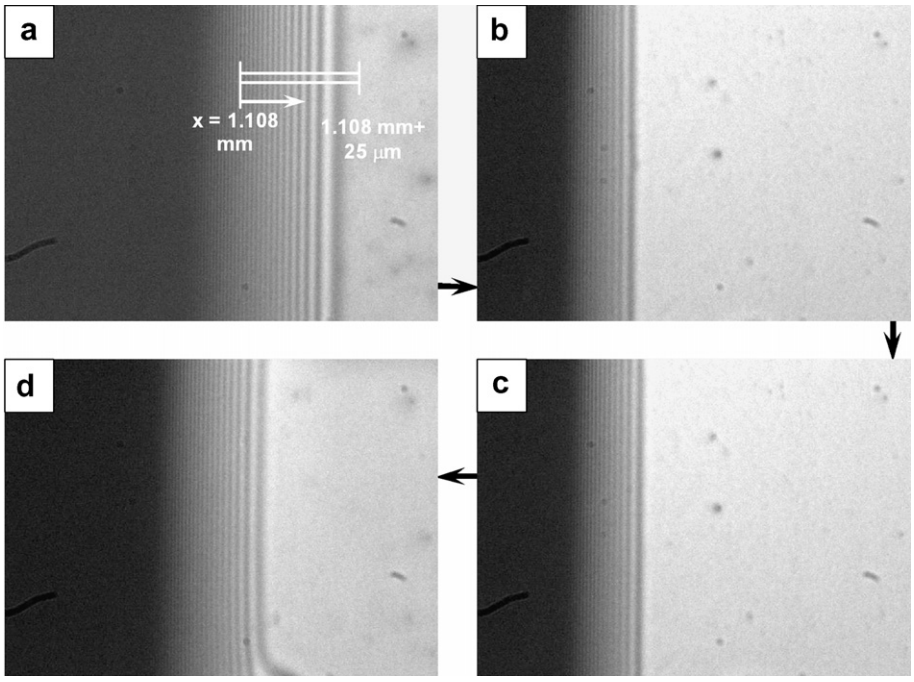

Fig. 2. Reflectivity images illustrating the movement of the pentane meniscus due to change in heater power: (a) isothermal state ($t = 0.07$ s), (b) receding state ($t = 8.4$ s), (c) advancing state ($t = 10.4$ s), and (d) pseudo-steady state ($t = 163.2$ s) [1].

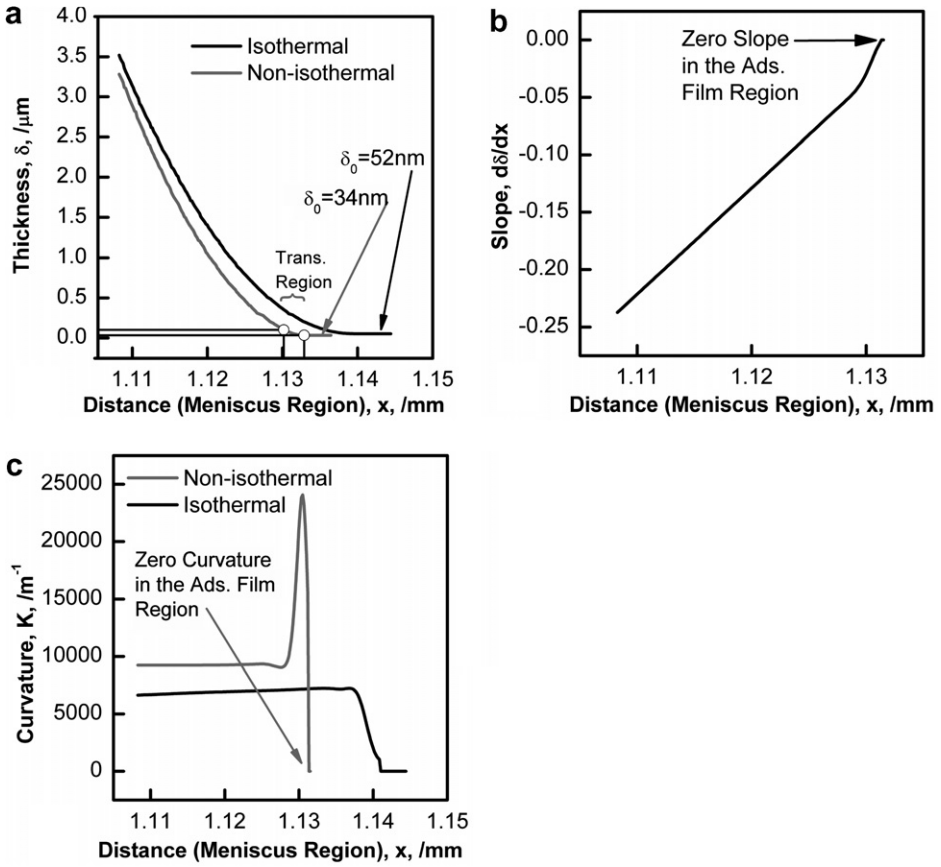

Fig. 3. Profiles for pentane: (a) thickness (isothermal state, t = 0.07 s; pseudo-steady state, t = 163.2 s), (b) slope (pseudo-steady state, t = 163.2 s) and (c) curvature (isothermal state, t = 0.07 s; pseudo-steady state, t = 163.2 s).

Due to the lack of high-resolution experimental data, researchers have been using a linear or constant curvature approximation in the transition region to model an evaporating meniscus (e.g., [12]). Thus, the details obtained here from the data analysis technique addresses the evaluation of these approximations. In addition, Panchamgam et al. [1–3] have experimentally shown that the transition region curvature profiles strongly depend on the purity of the fluid, Marangoni stresses and the solid–liquid interface temperature. To estimate the Marangoni stresses ($d\sigma/dx$), the temperature profiles (solid–liquid interface temperature (T_{sl}), the liquid–vapor interface temperature (T_{lv}), the vapor temperature (T_v)), the mass flow rate in the evaporating meniscus (Γ) and the evaporative heat flux at the liquid–vapor interface (q''_{ev}), two different models were developed. One model using the heat equation, referred to as the macro-model, represents the two-dimensional heat conduction in the solid (quartz cuvette), and the other model using continuum hydrodynamics, referred to as the micro-model, represents the details of the evaporating pentane meniscus over a length of 25 μm.

3. Theoretical formulation

The experimental system consists of two regions: (1) converging liquid flow in a micro-region with the measurement of the evaporating meniscus thickness, (34 nm < δ < 3.5 μm) over a length of 25 μm and (2) a macro-region with measurement of the outside surface temperature for the cuvette of length 43 mm and inside cross-section of 3 mm × 3 mm. The "macro-model" which consists of converging two-dimensional heat conduction in the solid (quartz cuvette) with the liquid–vapor evaporative flux being one of the boundary conditions (see Fig. 4) gives the solid–liquid interface temperature (T_{sl}). The "micro-model" for the liquid meniscus gives the flow rate (Γ), the Marangoni stresses ($d\sigma/dx$) and the liquid–vapor interface temperature (T_{lv}) profiles. The evaporative heat flux (q''_{ev}) profile, which serves as the boundary condition for the macro-model, is an output from the micro-model, and thus serves as the coupling variable between the two models. The theoretical details of the individual models are given in the following sections.

3.1. Two-dimensional heat conduction in the solid (macro-model)

In the literature, some of the theoretical models relating to the evaporation of a meniscus (e.g., [3,12]) assumed a constant solid–liquid interface temperature, thus ignoring the effect of thermal conduction in the solid on the solid–liquid interface temperature (T_{sl}). Herein, we find a non-constant temperature profile. Using different data, Stephan and Busse [13] also evaluated thermal conduction in the substrate. A change in the solid–liquid interface temperature would affect the evaporative heat removal rate at the liquid–vapor interface. To obtain the solid–liquid interface temperature, the following realistic model incorporating two-dimensional heat conduction in the walls of the cuvette was developed using a finite element approach. Fig. 4(a) defines the structure used to represent the square corner at the top end of the cuvette along with the two evaporating corner menisci formed near the inside corner (also, see Fig. 1). Fig. 4(b) shows the expanded region illustrating the inside corner of the cuvette where the evaporating menisci regions are replaced with the appropriate

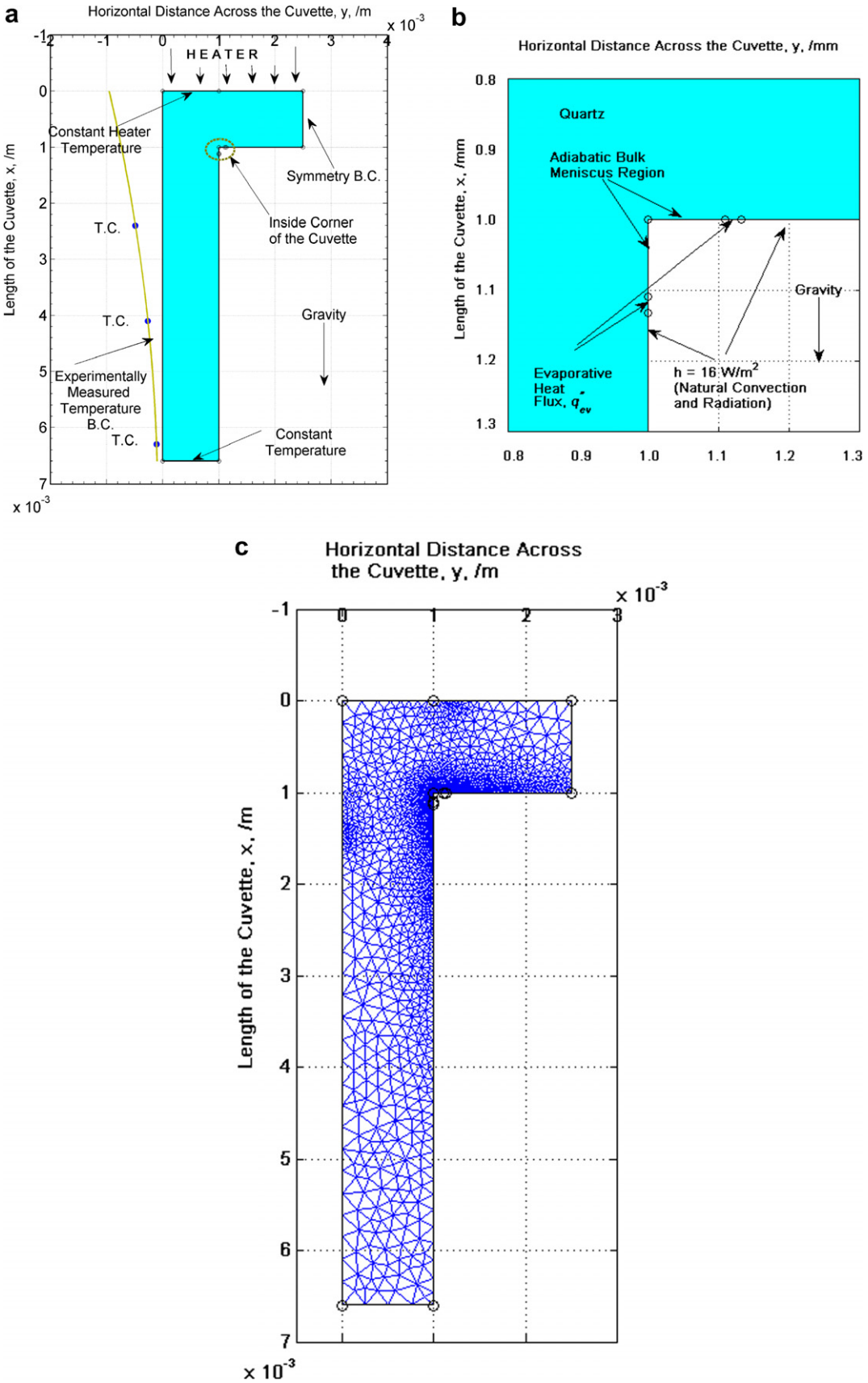

Fig. 4. (a) Finite-element model for two-dimensional heat conduction in the solid (quartz cuvette) with the imposed boundary conditions, (b) expanded view of the inside corner of the cuvette containing the evaporating pentane meniscus and (c) two-dimensional mesh structure defined for the solid (quartz cuvette).

boundary conditions. The boundary conditions imposed to solve the system defined in Fig. 4 are:

BC 1. At $x = 0$ and for all y representing the cuvette (along the heater at the outside top), we have a constant temperature condition, which is a standard boundary condition for a heater. The heater temperature was calculated to be 314.33 K by extrapolating the thermocouple readings taken along various points on outside surface of the cuvette, as shown in Fig. 4(a), where TC stands for thermocouple.
BC 2. At $y = 0$ and for all x representing the cuvette (the outside wall), a parabolic fit of the experimentally measured temperature profile was imposed, as shown in Fig. 4(a).
BC 3. At $y = 2.5$ mm (vertical central axis of the cuvette) and for $0 \leqslant x \leqslant 1$ mm, a zero heat flux across this boundary was imposed due to symmetry.
BC 4. At $x = 6.5$ mm and for $0 \leqslant y \leqslant 1$ mm (last thermocouple measurement), a constant temperature condition obtained from the experimentally measured temperature at $x = 6.5$ mm was used. The experimentally measured temperature at $x = 6.5$ mm was 305.9 K.
BC 5. For the inside corner of the cuvette, at $y = 1$ mm and for 1 mm $< x <$ 1.10826 mm, we have the adiabatic region representing the thicker meniscus region where evaporation is negligible (see Fig. 4(b)). Following the thicker meniscus region, an evaporating meniscus region or the heat sink is defined. Here, the q''_{ev} profile obtained from the continuum fluid-dynamics model and one-dimensional heat conduction in the liquid was used as the boundary condition. Also, the length of the evaporating portion of the meniscus region is determined from the measured meniscus length obtained from Fig. 3(a) ($\approx$25 μm). As the remaining distance inside the cuvette, $x >$ 1.10826 + 0.025 mm at $y = 1$ mm is exposed to the vapor of the working fluid and non-condensable gases, we would expect radiation and convective heat transfer, which, based on estimates by Wang [14], has a heat transfer coefficient of 16 W/m^2 K. Similar boundary conditions, as illustrated in Fig. 4(b), exist for the other solid–liquid interface at $x = 1$ mm and 1 mm $< y <$ 2.5 mm.

Using the above boundary conditions, the mesh structure defined in Fig. 4(c) was used to obtain the temperature profile. The structures were defined in a commercially available finite element solver, COMSOL®. COMSOL® used the steady state two-dimensional heat conduction equation in the quartz cuvette given by Eq. (1):

$$\nabla^2 T = 0 \quad \text{or} \quad \frac{d^2T}{dx^2} + \frac{d^2T}{dy^2} = 0 \tag{1}$$

where 'x' represents the length of the cuvette with $x = 0$ representing the heater end and 'y' represents the horizontal distance perpendicular to the length of the cuvette. For the COMSOL® to solve Eq. (1), in addition to the straightforward boundary conditions, BC 1–BC 4, as defined above, we need q''_{ev} (BC 5), which is obtained from the solution of the continuum hydrodynamic model in the micro-meniscus region. COMSOL® gives the converged solution for T_{sl} (solid–liquid interface temperature in the evaporating meniscus region), which is obtained from the two-dimensional temperature and heat flux distribution in the cuvette walls.

3.2. Continuum model for the evaporating meniscus (micro-model)

An evaluation of the heat transfer and temperature distribution in the Micro-meniscus region can be obtained from the measured thickness profile. The liquid pressure gradient profile to determine the variation of fluid flow is obtained from the thickness dependent pressure jump across the liquid–vapor interface as given by the following augmented Young–Laplace equation:

$$P_l(x) = P_{vT} - [\sigma(x)K(x) + \Pi(x)] \tag{2}$$

where P_{vT} is the total pressure in the vapor phase, P_l is the pressure in the liquid phase, K is the local curvature of the liquid–vapor interface, σ is the surface tension and Π is the disjoining pressure equal to $-B_{avg}/\delta^4$. Here B_{avg} (= 8.71×10^{-28} J m) is the experimentally obtained average retarded dispersion constant and is used because the resulting thickness of the adsorbed thin film region is thick enough to be in the retarded regime. These equations are valid in the meniscus region with x varying from 1108.26 μm $< x <$ 1108.26 + 25 μm. The measurement details of the average retarded dispersion constant are provided in Ref. [1]. We expect the disjoining pressure effect to be the primary influence in the adsorbed thin film region [1,11], where δ is small and the interface is flat giving zero curvature. On the other hand, we expect that the curvature effects will dominate in a large portion of the transition region ($\delta_0 < \delta <$ 0.1 μm, where δ_0 is the adsorbed film thickness) and the thicker meniscus region ($\delta >$ 0.1 μm) where the δ is large and curvature is non-zero and constant. In the initial portion of the transition region, there is a smooth transition between the disjoining pressure and curvature controlled regions. The vapor recoil pressure has been neglected.

To estimate the mass flow rate, the surface tension or Marangoni stresses, liquid–vapor interface temperature (T_{lv}) and the evaporative heat flux (q''_{ev}) profiles of the evaporating meniscus, we used the one-dimensional lubrication approximation to estimate the velocity $u(x,y)$, as given by Eq. (3):

$$\mu \frac{d^2u}{dy^2} = \frac{dP_l}{dx} \tag{3}$$

where μ is the dynamic viscosity of the pentane and 'y' is distance along the thickness of the meniscus. Eq. (3) was solved using the following boundary conditions:

$$\text{At} \quad y = 1 \text{ mm}, u_s = \beta \left.\frac{du}{dy}\right|_{y=1 \text{ mm}} \quad (\beta \text{ is the slip coefficient}) \tag{4}$$

$$y = \delta(x) + 1 \text{ mm}, \quad \tau_{yx} = \frac{d\sigma}{dx} \tag{5}$$

In Eq. (4), u_s represents a possible slip velocity at the solid–liquid interface. Based on the work by Park et al. [6] and others [5,15], we have used a Navier's partial slip boundary condition, which assumed that the velocity at the solid wall is proportional to strain rate at the solid surface. We found that a slip boundary condition was needed to obtain agreement between the macro-model results and the observed pressure profiles. This gives a higher flow rate than can be obtained from a no-slip condition. Wee et al. [12] have shown theoretically that the net heat flux increases with increasing slip due to additional fluid flow to the transition region. Thompson and Troian [16] proposed a correlation for the estimation of slip coefficient, β. However, for this current system, the correlation is not valid as the system is non-isothermal and the surface tension is not constant. Hence, a different method for the estimation of β, described later, was used. Eq. (5) equates the surface shear at the liquid–vapor interface to the surface tension gradient. These two boundary conditions can have large effects on the velocity profile, Eq. (6), and hence on the mass flow rate (Γ), Eq. (7)

$$u(x,y) = \frac{1}{\mu}\frac{dP_l}{dx}\left[\frac{y^2}{2} - y\delta\right] + \frac{y}{\mu}\sigma' - \frac{\beta}{\mu}\left[\delta\left(\frac{dP_l}{dx}\right) - \sigma'\right] \tag{6}$$

$$\Gamma(x) = \underbrace{\left[\left(\frac{K\delta^3\sigma'}{3\upsilon} + \frac{3\beta K\delta^2\sigma'}{3\upsilon}\right) + \left(\frac{\sigma\delta^3 K'}{3\upsilon} + \frac{3\sigma\delta^2\beta K'}{3\upsilon}\right)\right]}_{\text{TERM I CAPILLARITY}} + \underbrace{\left[-\frac{4(-B_{\text{avg}})\delta'}{3\upsilon\delta^2} - \frac{12\beta(-B_{\text{avg}})\delta'}{3\upsilon\delta^3}\right]}_{\text{TERM II DISJOINING PRESSURE}} + \underbrace{\left[\frac{1.5\delta^2\sigma'}{3\upsilon} + \frac{3\beta\delta\sigma'}{3\upsilon}\right]}_{\text{TERM III MARANGONI}} \quad (7)$$

where υ is the kinematic viscosity of the pentane and σ' is the liquid–vapor surface tension gradient along the length of the meniscus. The capillary term represents mass flow due to curvature effects, while the disjoining pressure term represents flow owing to the disjoining pressure, which is experienced primarily in the adsorbed thin film region. The Marangoni term reflects the effect of surface shear due to variation of surface tension with liquid–vapor interface temperature, T_{lv}, on the mass flow rate. The capillary term includes certain terms containing both $K\sigma'$. These terms have not been included in the Marangoni term because they arise from taking the derivative of the pressure term in Eq. (6) and are not an effect of the stress at the liquid–vapor boundary. The terms containing 'β' have been distributed based on how they affect the final mass flow rate. This becomes clear by noting that the last term in brackets in Eq. (6) simply adds an additional initial velocity to the corresponding terms from the first part. The surface tension (σ) and the kinematic viscosity (υ) in Eq. (7) depend on the liquid–vapor interface temperature as

$$\sigma = a + bT_{\text{lv}} \quad (8)$$

$$\upsilon = f(T_{\text{lv}}) \quad (9)$$

The correlation function for μ (= $\upsilon\rho_{\text{l}}$, where ρ_{l} is pentane density), and the parameters a and b for pentane are from [17]. The temperature profile was obtained by assuming one-dimensional heat conduction in the liquid in the 'y' direction. Under these assumptions, the temperature at the liquid–vapor interface is given as

$$T_{\text{lv}} = T_{\text{sl}} - \frac{q''_{\text{ev}}\delta}{k_{\text{l}}} \quad (10)$$

$$q''_{\text{ev}} = -h_{\text{fg}}\frac{\mathrm{d}\Gamma}{\mathrm{d}x} \quad (11)$$

where T_{sl} is the solid–liquid interface temperature obtained from the solution of the two-dimensional heat conduction in the cuvette walls using COMSOL®, k_{l} is the thermal conductivity of pentane and q''_{ev} is the evaporative heat flux at the liquid–vapor interface in the micro-meniscus region. Using Eq. (11) we can calculate the local evaporative heat flux, which was obtained by assuming that the difference in the mass flow rates ($\mathrm{d}\Gamma$) across a control volume of the meniscus of width '$\mathrm{d}x$' is solely due to evaporation.

Eqs. (7)–(11) were numerically solved, using the experimental values of δ, δ', K' and calculated values of T_{sl}, to obtain β, T_{lv}, σ, Γ and q''_{ev}. The problem is under defined with the extra variable β (slip coefficient). Hence the complete solution is obtained iteratively by varying the value of β such that convergence in T_{sl} is obtained. The slip coefficient was found to be $\beta = 100 \times 10^{-9}$ m or 100 nm. The significance of the slip coefficient is discussed later.

3.3. Kelvin–Clapeyron model

For non-equilibrium systems, using interfacial kinetic theory, Eq. (12) was derived for the interfacial mass flux (m'' or $\mathrm{d}\Gamma/\mathrm{d}x$) written as a net heat flux associated with interfacial condensation or evaporation (e.g., [18,19]). Eq. (12) includes both the effect of an interfacial temperature jump (Clapeyron effect, superscript 'cl') and the interfacial pressure jump (Kelvin effect, superscript 'kl') on the interfacial heat flux (q''_{ev}):

$$q''_{\text{ev}} = m''\Delta h_{\text{m}} = h_{\text{lv}}(T_{\text{lv}} - T_{\text{v}}) = h^{\text{cl}}_{\text{lv}}(T_{\text{lv}} - T_{\text{v}}) - h^{\text{kl}}_{\text{lv}}(\Pi + K\sigma) \quad (12)$$

where

$$h^{\text{kl}}_{\text{lv}} = \left(\frac{C^2M}{2\pi R_{\text{g}}T_{\text{lv}}}\right)^{1/2}\frac{V_{\text{lm}}P_{\text{v}}\Delta h_{\text{m}}}{R_{\text{g}}T_{\text{lv}}} \quad \text{and}$$

$$h^{\text{cl}}_{\text{lv}} = \left(\frac{C^2M}{2\pi R_{\text{g}}T_{\text{lv}}}\right)^{1/2}\frac{MP_{\text{v}}\Delta h^2_{\text{m}}}{R_{\text{g}}T_{\text{lv}}T_{\text{v}}} \quad (13)$$

where Δh_{m} is the latent heat of vaporization per unit mass, R_{g} is the gas constant and C is the constant of proportionality. Using Eqs. (12) and (13), we obtained the vapor temperature (T_{v}) profile for the current experimental system containing pentane as the working fluid. As the pentane meniscus length is approximately 25 μm and due to the lack of high-resolution temperature measuring devices, we used the combination of modeling (two-dimensional heat conduction in the solid, one-dimensional heat conduction in the liquid and kinetic theory at the liquid–vapor interface) and experimental data (δ, δ', K, K' and the wall temperature) to obtain the variation in the vapor temperature as a function of the meniscus length.

4. Algorithm scheme

Fig. 5 represents the flow chart of the algorithm used in this work. Initially, for the first iteration, $i = 1$, we assume the solid–liquid interface temperature is the same as the outside wall temperature at the meniscus location (or at $y \approx 1$ mm). Using the micro-model, we obtain the evaporative heat flux (q''_{ev}) in addition to the mass flow rate per unit width (Γ), the surface tension gradient ($\mathrm{d}\sigma/\mathrm{d}x$) and the liquid–vapor interface temperature (T_{lv}) profiles at

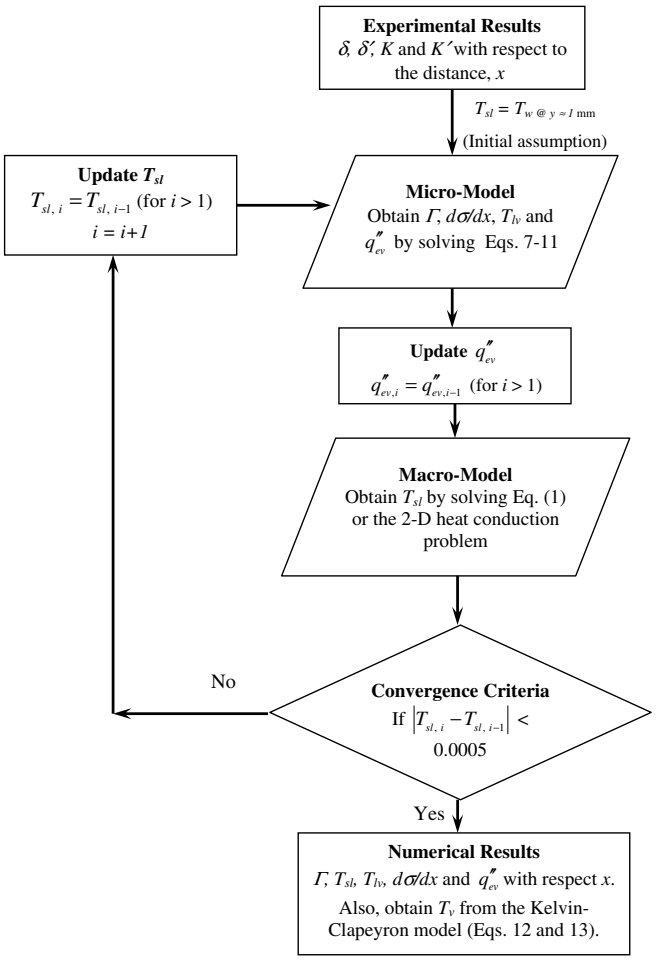

Fig. 5. Flowchart representing the algorithm scheme used to solve the macro-model and the micro-model.

the liquid–vapor interface. The evaporative heat flux obtained from the micro-model establishes one of the boundary conditions (BC 5) for the macro-model to solve for the two-dimensional solid heat conduction (Eq. (1)). The macro-model yields the temperature and the heat distribution in the solid and calculates the solid–liquid interface temperature (T_{sl}), which is input to the next iteration ($i = i + 1$) of the micro-model. The loop between the micro-model and macro-model continues until the convergence criterion is met. The criterion used for the convergence is that the absolute difference in $T_{sl,}$ the solid–liquid interface temperature between consecutive iterations should be less than 0.0005. When the convergence criteria is satisfied, the programs come out of the loop to give us the solution of the complete set of variables, i.e., $T(x,y)$, T_{sl}, T_{lv}, T_v (from Eqs. (12) and (13)), Γ, β, σ, $d\sigma/dx$ and q''_{ev}.

5. Results and discussion

5.1. Temperature and heat flux distribution in the solid from the two-dimensional solid conduction model (macro-model)

Fig. 6 shows the heat flow and isotherm distribution in the solid (quartz cuvette). Since the evaporating pentane meniscus is a strong heat sink, we find most of the heat flow converging into the microscopic evaporating meniscus region of length 25 μm. This demonstrates that an evaporating meniscus can significantly improve the heat transfer and heat removal properties of a solid. This also demonstrates the effect of the overall system configuration on the heat flow profile.

Fig. 7(a) shows the plot of the temperature profile at the inside surface, $y = 1$ mm, along the length of the cuvette, x. We observed a dip in the temperature in the evaporating meniscus region (dotted ellipse), which is due to the significant heat transfer that occurs in this part of the meniscus formed near the corner of the cuvette. The details of the dip in the solid–liquid interface temperature are clearly shown in Fig. 7(b), where the circles represent the evaporating meniscus region. On the left side of the evaporating meniscus, we have the adiabatic thicker meniscus region, which has a very low evaporation flux due to the higher orders of the liquid film thickness. On the right side of the evaporating meniscus, we have the solid–liquid film-vapor layer, where the liquid film is the adsorbed film region of constant thickness 34 nm. The numerically obtained temperature profile dip at the solid–liquid interface is similar to the experimental findings of Sodtke et al. [4]. Hence, the dip in the temperature profile at the solid–liquid interface not only emphasize the heat sink characteristics of an evaporating meniscus, but also gives more insight on the actual temperature profiles that exist at these microscopic regions. Additional temperature profiles are given below.

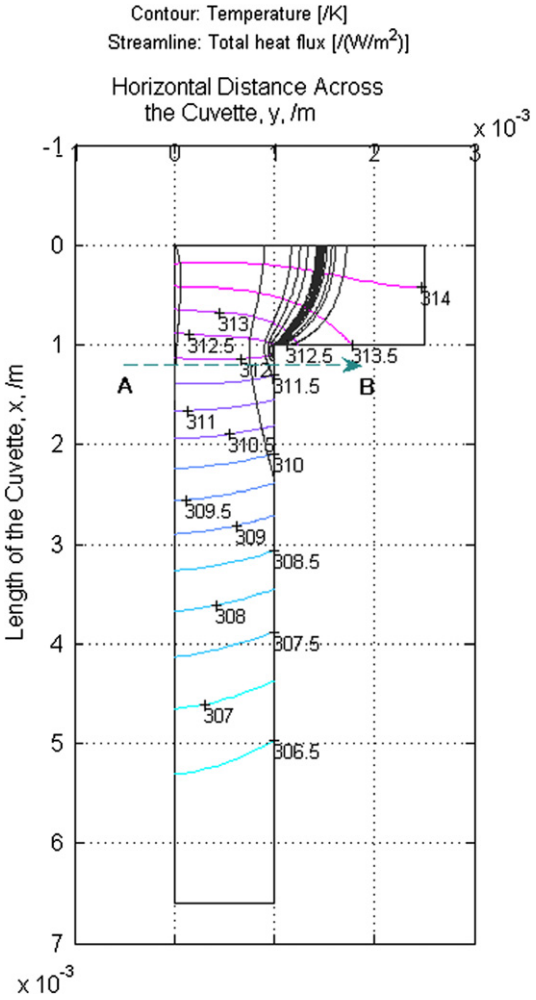

Fig. 6. Heat flux and isotherms through the solid (quartz cuvette). The heat flow in the solid converges into the evaporating pentane meniscus region.

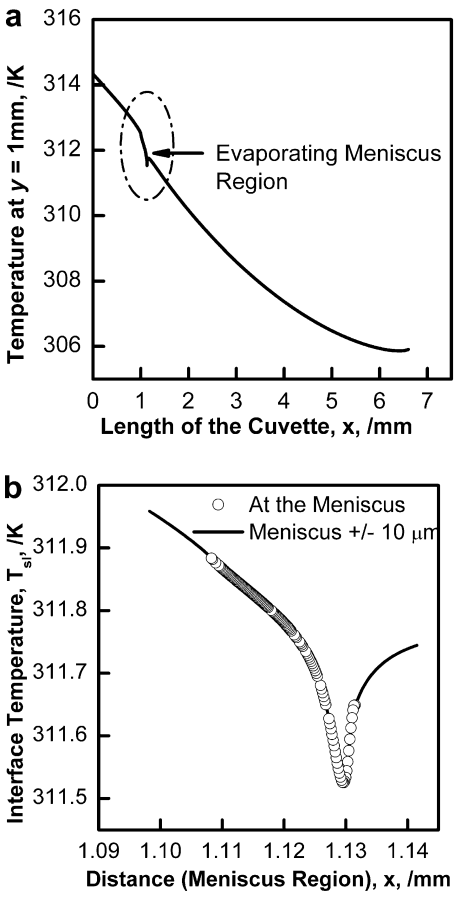

Fig. 7. (a) Solid interface temperature profiles at $y = 1$ mm. (b) Solid–liquid interface temperature profiles in the vicinity of the evaporating meniscus region (dotted ellipse in (a)). Circles represent the evaporating pentane meniscus region (see (b)). The solid line on the left of the evaporating meniscus represents the adiabatic meniscus region. The solid line on the right of the evaporating meniscus represents the solid–liquid–vapor interface, where the liquid film is the thin adsorbed film.

5.2. Mass flow rate per unit width (Γ)

Fig. 8(a) shows the mass flow rate per unit width as a function of the distance (x). The mass flow rate is zero in the adsorbed film region, then changes rapidly in the transition region and reached a maximum value of 0.1×10^{-5} kg/m s. A small dip is observed adjacent to the adsorbed thin film, which might be a numerical artifact or might be due to recirculation similar to the one predicted by Goodwin and Homsy for fluids flowing down an incline [20]. In comparison, binary mixture containing small quantities of higher molecular weights have higher mass flow rates compared to pure fluids due to more favorable Marangoni stresses (flow due to surface tension gradient) [3]. However, for the pure fluids, it is found that Marangoni stresses hinder the fluid flow rate in a portion of the meniscus, in particular, in the transition region.

From Eq. (7), we obtained the individual component contributions due to capillary pressure, disjoining pressure and Marangoni stress to the mass flow rate. A comparison of the three terms is shown in Fig. 8(b). A positive value of these terms is favorable for fluid flow towards the adsorbed film region. By definition, the sign of these terms depends on the signs of δ, δ', K, K' and σ'. For a completely wetting meniscus like pentane on a quartz surface, δ' is negative. Hence the contribution of the disjoining pressure term is positive. For an adsorbed film thickness of the non-isothermal evaporating pentane meniscus that is really low like 34 nm where the disjoining pressure is high, the results presented herein agree with the experimental findings in Ref. [1]. In Fig. 8(b), we see that, the capillary term is positive and contribute to the mass flow rate or evaporation in the transition region, consistent with the literature and previous experimental results [1,2]. It is interesting to note the large Marangoni term in the bulk meniscus region (1.11 to ~1.125 mm), showing that the flow is primarily due to thermocapillarity. The term however, changes sign, and is negative in the transition region ($\delta_0 < \delta < 0.1$ μm), where most of the evaporation takes place. This demonstrates that, for pure fluids, surface tension at the liquid–vapor interface enhances the mass flow rate and, in turn, the evaporation in the bulk meniscus region. On the other hand, it hinders it in the transition region. This variation in the surface tension gradient in the transition region is mainly due to the change in the liquid–vapor interface temperature profile, which depends on the thickness, slope, and curvature of the meniscus and on the temperature at the solid–liquid interface.

5.3. Liquid–vapor interface temperature (T_{lv})

Fig. 9(a) compares the liquid–vapor interface temperature (T_{lv}) profile with respect to the solid–liquid interface temperature (T_{sl}). We see a significant dip in the liquid–vapor interface temperature profile in the transition region. The observed dip in the T_{lv} depends mainly on the dip in the solid–liquid interface temperature, which is due to significant heat removal in the transition region due to evaporation: the thickness of the liquid film in the transition region is optimum and offers the least resistance for evaporation. We also observe that, for higher thicknesses (lower values of x), the liquid–vapor interface temperature does not significantly change with the change in the solid–liquid interface temperature. This is attributed to the resistance for heat conduction in the liquid film.

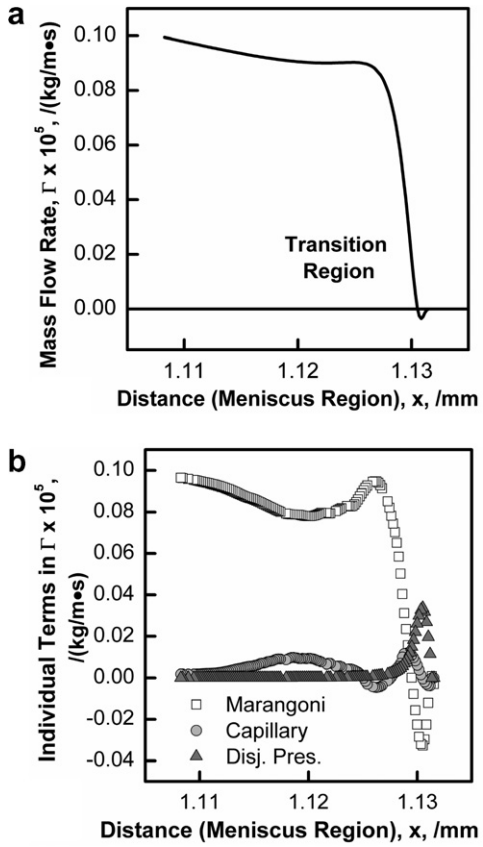

Fig. 8. (a) Mass flow rate per unit width of the meniscus as a function of the meniscus length during evaporation and (b) comparison of the individual terms that contribute to the mass flow rate (Eq. (7)).

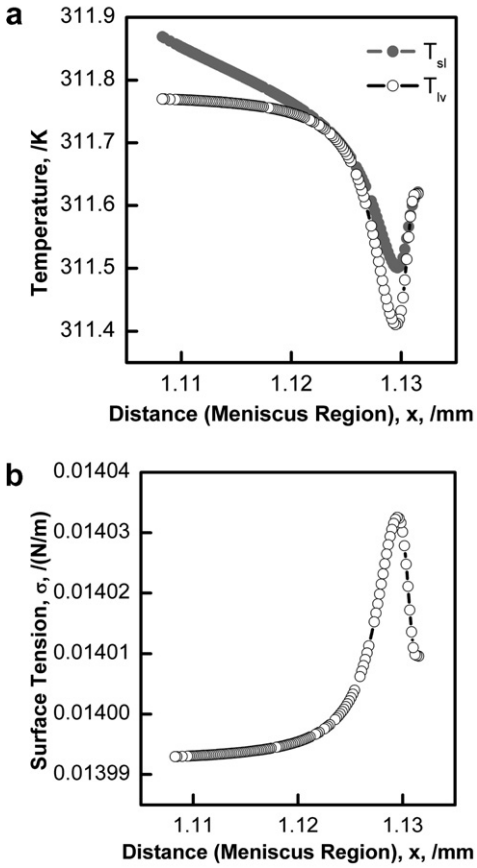

Fig. 9. (a) The solid–liquid and liquid–vapor interface temperature profiles in the evaporating meniscus region as a function of the meniscus length and (b) surface tension variation with the evaporating meniscus region.

5.4. Surface tension (σ_{lv})

Fig. 9(b) represents the variation in the surface tension of the liquid–vapor interface along the length of the evaporating meniscus. In the adsorbed film region, $x \to 1.13$ mm, the surface tension is equal to 14.01×10^{-3} N/m. In the transition region, the surface tension showed a maximum, which is due to the dip in the liquid–vapor interface temperature. The minimum in the surface tension caused the change in the sign of the Marangoni stress discussed above.

5.5. Heat flux distribution in the solid and local evaporative heat flux at the liquid–vapor interface

A plot of the heat flux variation at $y = 1$ mm along the length of the cuvette (x) is shown in Fig. 10(a). The profile shows a spike in the heat flux in the evaporating meniscus region. Fig. 10(b) shows the details of the spike in the local evaporative heat flux distribution along the length of the evaporating pentane meniscus. In the adsorbed film region ($x \to 1.13$ mm), the evaporative heat flux is zero due to the strong resistance for evaporation from the disjoining pressure or attractive forces between the liquid and the underlying substrate. In the thicker meniscus region ($x \to 1.11$ mm), the evaporation at the liquid–vapor interface is very small due to the higher resistance for heat conduction. In the transition region, the thickness of the film is optimum, and hence we see a maximum in the evaporative heat flux. Again, similar to the depression in mass flow rate per unit length (Γ), a dip is observed near the adsorbed thin film, which could be due to recirculation at the contact line. The average evaporative heat flux in the evaporating meniscus region is $q''_{ev,avg} = 1.68 \times 10^4$ W/m^2. Of course, higher heat fluxes are obtainable but more difficult to study. The presented results emphasize the use of the measured thickness profile.

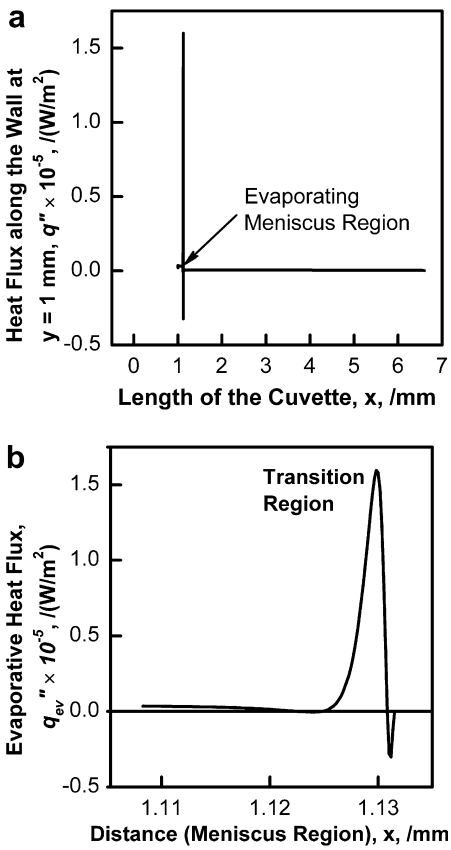

Fig. 10. (a) Heat flux profile at $y = 1$ mm and (b) evaporative heat flux profile at the liquid–vapor interface of the evaporating meniscus region.

5.6. Temperature profiles in the meniscus region

There are two potential jumps at the liquid–vapor interface: temperature and total pressure. We take the total pressure in the vapor to be a constant and allow a temperature and vapor pressure variation in the vapor. Using the Kelvin–Clapeyron equation, we obtained the vapor temperature (T_v) profile and a plot of the variation of T_v as a function of the evaporating meniscus length is shown in Fig. 11. We see that the vapor temperature is non-uniform and less than the liquid–vapor interface temperature. In addition, we see a dip in the vapor temperature in the transition region of the evaporating meniscus, which implies a strong dependence of T_v on the liquid–vapor interface temperature or on the solid–liquid interface temperature due to the resistance at the liquid–vapor interface. Also, the decrease in the vapor temperature in the transition region could be due to the consumption of latent heat of vaporization in this region. Also plotted in Fig. 11 are various temperature profiles in the vicinity of the evaporating meniscus, starting from the outside (experimentally measured) wall temperature through the solid (quartz cuvette), solid–liquid interface, liquid–vapor interface and the vapor temperature (represented by the dotted line in Fig. 6). We observe that, the experimentally measured outside wall temperature (T_w) profile is linear along this small length. In addition, the temperature profiles in the solid close to the solid–liquid interface, i.e., $T_{sl\text{-}0.1\ mm}$, which is 0.1 mm from the solid–liquid interface and $T_{sl\text{-}10\ \mu m}$, which is 10 μm from the solid–liquid interface, shown in Fig. 11, exhibit almost linear profiles as well. However, as we approach the solid–liquid interface, the temperature profiles deviate from the linear behavior and start showing a dip in the transition region of the evaporating meniscus (see $T_{sl\text{-}1\ \mu m}$ in Fig. 11). The dip was also observed for T_{sl}, T_{lv}, and T_v, and is due to the significant heat removal in the transition region. Hence, only external temperature profiles in a miniature heat pipe would not give the complete understanding of the heat removal process described above.

5.7. Shear stress at the solid–liquid interface and slip coefficient

To obtain closure between the macro- and micro-models, the inclusion of a slip velocity at the liquid–solid interface was needed.

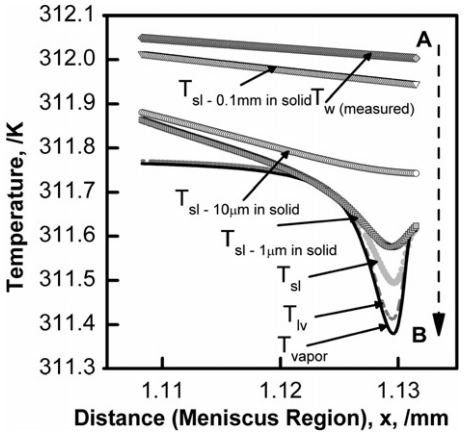

Fig. 11. Temperature profiles in the evaporating meniscus region. A to B represents the direction from outside of the cuvette into the evaporating meniscus region (see Fig. 6).

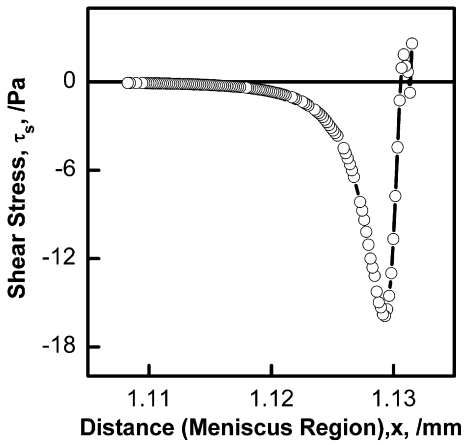

Fig. 12. Shear stress at the solid–liquid interface in the evaporating meniscus region.

Fig. 12 shows the shear stress at the solid–liquid interface at the evaporating meniscus region. For a similar system, Spikes and Granick have demonstrated slip using a simple isothermal non-evaporating fluid on a completely wetting surface in a SFA [5]. They have proposed a critical shear stress value of 6 Pa based on their experiments, a value which is exceeded in sections of the evaporating meniscus. Schmatko et al. [21] experimentally probed the flow velocity of hexadecane at various solid interfaces using a fluorescence recovery after photobleaching (FRAP) technique. They found that for shear rates in the range of 200–2000 s^{-1}, hexadecane slips on a completely wetting bare sapphire glass, and the corresponding slip coefficient was 175 nm (±50 nm). In our case, the value of slip coefficient (100 nm) obtained numerically was lower than [21], but comparable to the experimentally observed slip coefficient for a wetting system. While the presence of slip is not conclusively proven here, it seems necessary to obtain sensible results from the experimental data. The vapor recoil pressure was calculated to be 3×10^{-4} Pa, at the position of maximum shear stress justifying our neglecting it in the formulation.

6. Conclusions

This study of an evaporating meniscus is unique in that experimental thickness profile data and temperature measurements have been used directly to obtain heat flux and mass flow rate with very high resolution. The following results have been demonstrated:

1. Since transport processes in the contact line region depend on many variables, both detail experimental data and complementary modeling are needed to fully understand the processes.
2. The feasibility of using a continuum fluid-dynamics "micro" model based on high-resolution experimental data along with a two-dimensional finite element heat conduction "macro" model was demonstrated.
3. The mass flow rate per unit width, Γ, decreases sharply in the transition region indicating that the maximum evaporation rate and evaporative heat flux, q''_{ev}, occurs in this region.
4. Slip has been predicted at the solid–liquid interface to explain the high mass flow rates observed in the evaporating pentane meniscus.
5. There is a sharp dip in the solid–liquid interfacial temperature profile in the meniscus region demonstrating that the evaporating meniscus acts as a large heat sink. This insight into the solid–liquid interface temperature profile was made possible by including the effect of heat conduction in the solid substrate. The outside solid surface temperature also shows a dip due to the presence of the heat sink.
6. The possibility of a non-uniform vapor temperature has been explored. It is proposed that the vapor temperature, as obtained by the Kelvin–Clapeyron model, shows a dip in the evaporating region.
7. Depending on the liquid thickness, Marangoni stresses can either enhance or hinder fluid flow towards the contact line for the evaporating pure pentane meniscus. Marangoni stress has been shown to be significant in fluid transport in the bulk meniscus region.

Acknowledgements

This material is based on the work supported by the National Aeronautics and Space Administration under grant number NNC05GA27G. Any opinions, findings, and conclusions or recommendations expressed in this publication are those of the authors and do not necessarily reflect the view of NASA.

References

[1] S.S. Panchamgam, J.L. Plawsky, P.C. Wayner Jr., Microscale heat transfer in an evaporating moving extended meniscus, Exp. Therm. Fluid Sci. 30 (2006) 745–754.
[2] S.S. Panchamgam, J.L. Plawsky, P.C. Wayner Jr., Experimental evaluation of Marangoni shear in the contact line region of an evaporating 99+% pure octane, J. Heat Transfer Special Issue Nanochannels, Microchannels Minichannels 129 (2007) 1476–1485.
[3] S.S. Panchamgam, J.L. Plawsky, P.C. Wayner Jr., Spreading characteristics and microscale evaporative heat transfer in an ultrathin film containing a binary mixture, J. Heat Transfer Special Issue Boil Interf Phenom 128 (12) (2006) 1266–1275.
[4] C. Sodtke, J. Kern, N. Schweizer, P. Stephan, High resolution measurements of wall temperature distribution underneath a single vapour bubble under low gravity conditions, Int. J. Heat Mass Transfer 49 (5–6) (2006) 1100–1106.
[5] H. Spikes, S. Granick, Equation for slip of simple liquids at smooth solid surfaces, Langmuir 19 (2003) 5065–5071.
[6] K. Park, K.J. Noh, K.S. Lee, Transport phenomena in the thin-film region of a micro-channel, Int. J. Heat Mass Transfer 46 (2003) 2381–2388.
[7] S.K. Wee, K.D. Kihm, K.P. Hallinan, Effects of the liquid polarity and the wall slip on the heat and mass transport characteristics of the micro-scale evaporating transition film, Int. J. Heat Mass Transfer 48 (2) (2005) 265–278.
[8] M. Potash Jr., P.C. Wayner Jr., Evaporation from a two-dimensional extended meniscus, Int. J. Heat Mass Transfer 15 (7) (1972) 1851–1863.
[9] B.V. Derjaguin, N.V. Churaev, The definition of disjoining pressure and its importance in the equilibrium and flow of thin films, Colloid J. USSR 38 (1976) 438–448.
[10] B.V. Derjaguin, Z.M. Zorin, Optical study of the adsorption and surface condensation of vapours in the vicinity of saturation on smooth surface, in: Proceedings of the Second International Conference on Surface Activity, vol. 2, 1957, pp. 145–152.
[11] S.S. Panchamgam, S.J. Gokhale, J.L. Plawsky, S. DasGupta, P.C. Wayner Jr., Experimental determination of the effect of disjoining pressure on shear in the contact line region of a moving evaporating thin film, J. Heat Transfer 127 (2005) 231.
[12] S.K. Wee, K.D. Kihm, D.M. Pratt, J.S. Allen, Microscale heat and mass transport of evaporating thin film of binary mixture, J. Thermophys. Heat Transfer 20 (2) (2006) 320.
[13] P.C. Stephan, C.A. Busse, Analysis of the heat transfer coefficient of grooved heat pipe evaporator walls, Int. J. Heat Mass Transfer 35 (2) (1992) 383–391.
[14] Y.X. Wang, A study of the vertical constrained vapor bubble, Ph.D. Thesis, Rensselaer Polytechnic Institute, Troy, NY, 2001.
[15] E. Lauga, M.P. Brenner, H.A. Stone, Microfluidics: the no-slip boundary condition, in: J. Foss (Ed.), Handbook of Experimental Fluid Dynamics, Springer-Verlag, Berlin, 2005.
[16] P.A. Thompson, S.M. Troian, A general boundary condition for liquid flow at solid surfaces, Nature 389 (6649) (1997) 360.
[17] CRC Handbook of Chemistry and Physics, 84th ed., CRC Press, Boca Raton, 2003.
[18] S. DasGupta, I.Y. Kim, P.C. Wayner Jr., Use of the Kelvin–Clapeyron equation to model an evaporating curved microfilm, J. Heat Transfer 116 (4) (1994) 1007.
[19] L.W. Swanson, G.P. Peterson, The interfacial thermodynamics of micro heat pipes, J. Heat Transfer 115 (1995) 195–201.
[20] R. Goodwin, G.M. Homsy, Viscous flow down a slope in the vicinity of a contact line, Phys. Fluids A 3 (4) (1991) 515–528.
[21] T. Schmatko, H. Hervet, L. Léger, Effect of nanometric-scale roughness on slip at the wall of simple fluids, Langmuir 22 (2006) 6843–6850.